Geothermics 96 (2021) 102204

Contents lists available at ScienceDirect

Geothermics

journal homepage: www.elsevier.com/locate/geothermics

Down-dip circulation at the united downs deep geothermal power project maximizes heat recovery and minimizes seismicity

Quan Gan [a,c,d], Zijun Feng [c], Lei Zhou [a,*], Honglian Li [a], Jun Liu [e], Derek Elsworth [b]

[a] State Key Laboratory of Coal Mine Disaster Dynamics and Control, Chongqing University, Chongqing, China
[b] Department of Energy and Mineral Engineering, EMS Energy Institute and G3 Center, Pennsylvania State University, University Park, Pennsylvania, United States
[c] Key Laboratory of In-situ Property-Improving Mining of Ministry of Education, Taiyuan University of Technology, Taiyuan, Shanxi 030024, China
[d] School of Geosciences, University of Aberdeen, United Kingdom
[e] Institute of New Energy and Low-Carbon Technology, Sichuan University, Chengdu 610065, China

ARTICLE INFO

Keywords:
United downs deep geothermal project
Well pattern
Induced seismicity
Fault reactivation

ABSTRACT

Fault damage zones potentially represent native permeable channels within otherwise ultra-tight igneous formations that may be used to promote fluid circulation for convective heat recovery. The United Downs Deep Geothermal Power (UDDGP) project aims to recover geothermal energy by directly injecting, circulating then recovering fluids from such a fault. The UDDGP project injects fluid into the fault at 2500 m where rock temperature is ~75 °C – 80 °C and recovers the injectate from 4500 m, where the bottom hole temperature is predicted to be 190 °C. We explore such down-dip circulation through numerical modeling to determine the anticipated temperature and longevity of the thermal recovery and the potential for induced seismicity (fault reactivation) by contrasting response for up-dip circulation. The results reveal that down-dip circulation not only maximizes water temperature and flow rate at the outlet but also simultaneously suppresses fault reactivation over the long term. In down-dip circulation, fault permeability in the critically stressed shallow fault damage zone is more greatly enhanced than that of the deep fault as a result of the strong injection-induced thermal stress. Fault sealing is breached as a result of reactivation in the shallow fault, prompting transverse fluid penetration and subsequent fluid circulation in the footwall. Switching the injection scheme from down-dip circulation to up-dip circulation, while maintaining an identical injection rate, leads to a drastic increase in the cumulative number of seismic events, with the average magnitude increasing from 1 to 2. This reversed well configuration (circulation bottom to top) also reduces power output from 6 to 7 $MW_{thermal}$ to 2 $MW_{thermal}$, due to reduced enthalpy and flow rate in the production well. The outcomes from this study confirm the preferred design of the well pattern as circulating top to bottom, to both maximize heat recovery and limit induced seismicity. A lower production pressure is necessary to avoid pressure build-up inside the fault . Production pressure at 15–20 MPa could ensure both high cumulative power generation and a stable fault state.

1. Introduction

Fault reactivation presents a potential hazard in the recovery of hydrocarbons and geothermal fluids (Kim et al., 2018; Wiprut and Zoback, 2000; Donnelly, 2006; Juncu et al., 2020). Significant effort has been applied to understand the physics of fault reactivation including considerations of rate and state friction (Ruina, 1983, Scholz, 1998) or brittle Coulomb friction (Q. Gan and Elsworth, 2014a; Rinaldi et al., 2015) and including impacts of healing (Wu et al., 2017; Wang and Elsworth, 2016) and dilatant hardening (Samuelson et al., 2009). Slip velocity directly impacts peak friction after healing (Marone, 1998) with stress state and healing influenced by thermomechanical and thermochemical effects (Taron and Elsworth, 2009; Q. Gan and Elsworth, 2014b). Pressure changes caused by fluid injection or extraction further alters effective stress state and rock properties (porosity and permeability) (Ellsworth, 2013; Segall and Lu, 2015; Gan and Elsworth, 2015) as does thermal unloading (Gan and Lei, 2020; Vilarrasa et al., 2015).

Seismicity is known to effect the permeability structure of faults (Manga, et al., 2012; Cappa and Rutqvist, 2012; Q. Gan and Elsworth, 2016). Shear dilation exerts a first-order impact on permeability (Min et al., 2004; Min and Jing, 2003; Q. Gan and Elsworth, 2016b) with permeability and frictional response further mediated by fault

* Corresponding author.
E-mail address: zhoulei84@cqu.edu.cn (L. Zhou).

https://doi.org/10.1016/j.geothermics.2021.102204
Received 13 October 2020; Received in revised form 3 June 2021; Accepted 30 June 2021
Available online 10 July 2021

roughness and slip rate. For high roughness fractures, permeability evolves episodically due to cycled compaction and dilation during shearing (Fang et al., 2018). Consequently, permeability evolution is correlated with fault frictional strength and mediated by sliding velocity and mineralogy (Fang et al., 2017).

Given the difficulty in creating enduring permeable pathways in otherwise low permeability rocks, the benefits of utilizing preexisting and resilient permeable conduits are clear. A variety of projects have demonstrated the feasibility of utilizing dormant fault zones to recover geothermal energy (Moeck et al., 2015; Rosberg et al., 2019; Gischig et al., 2020; Anyim and Gan, 2020). The work reported in the following is placed in the context of the United Downs Deep Geothermal Power (UDDGP) project, located near Redruth in west Cornwall, UK. It is within this context that we explore the feasibility of direct injection into, and recovery from, a fault zone. We highlight potential issues related to injection-induced fault reactivation for the specific geometry and characteristics of the United Downs Deep Geothermal Power (UDDGP) project. The coupled thermal-hydro-mechanical-chemical simulator TOUGHREACT-FLAC^{3D} is used to define the spatial and temporal evolution of fault permeability structures and associated efficiency of energy recovery over the long-term lifetime of the project. Different stimulation and production scenarios are analyzed to examine the potential for induced seismicity, in terms of timing, location, and magnitude. The implications from this work provide fundamental guidance for projects involving fluid injection into preexisting faults to recover geothermal fluids.

2. Field geologic setting

The UDDGP is located near Redruth in Cornwall, UK., close to the former Hot Dry Rock (HDR) geothermal research project at Rosemanowes (c. 1980s) (Parker, 1999). Cornwall has the highest geothermal gradient in the UK, with the Cornubian Batholith elevating heat flow to +125 mW/m^2, compared to the UK average of 54 mW/m^2. Surface heat flux at United Downs is anticipated to be ~120 mW/m^2 (Ledingham et al., 2019). The potential geothermal target is the Porthtowan Fault (PTF) - one of the northwest-southeast striking fault zones that are present throughout Cornwall (Fig. 1). The architecture of the PTF is >15 km long and 200 m – 500 m wide, striking NNW-SSE. The target PTF extends from Porthtowan on the north coast to Falmouth on the south coast along the northeast side of the Carnmenellis granite. Some of northwest-southeast striking faults are assumed to have been generated during the pre-orogenic Devonian extensional phase and followed by phases of fault reactivation and enhanced permeability resulting from intrusion of the late to post-orogenic granitic melts which now form the Cornubian granitic batholith (Ledingham et al., 2019).

The concept of the UDDGP development is to drill two deviated wells that pierce the fault at different vertical depths – both sourcing from a well-pad at the surface within the United Downs Industrial Estate. The injection well is scheduled to pump water at a flow rate between 20 and 60 kg/s and temperature of 75 °C. The initial temperature of the rock near injector is approximately 130 °C (Fig. 2). Preexisting highly permeable channels in the fault zones could potentially support a configuration with large well spacing and also ensure high flow rate circulation from injector to production well without significant fluid loss. Consequently, there is significant importance to explore the role of fault permeability in the efficiency of heat energy extraction and to examine the particulars of the injection recovery geometry and converse configurations.

3. Methodology and conceptual model

We evaluate the fluid circulation, heat transfer and associated deformation response for the UDDGP using the fully coupled Thermal-Hydraulic-Mechanical-Chemical simulator TOUGHREACT-FLAC^{3D}. This simulator has been extensively validated/calibrated and applied to

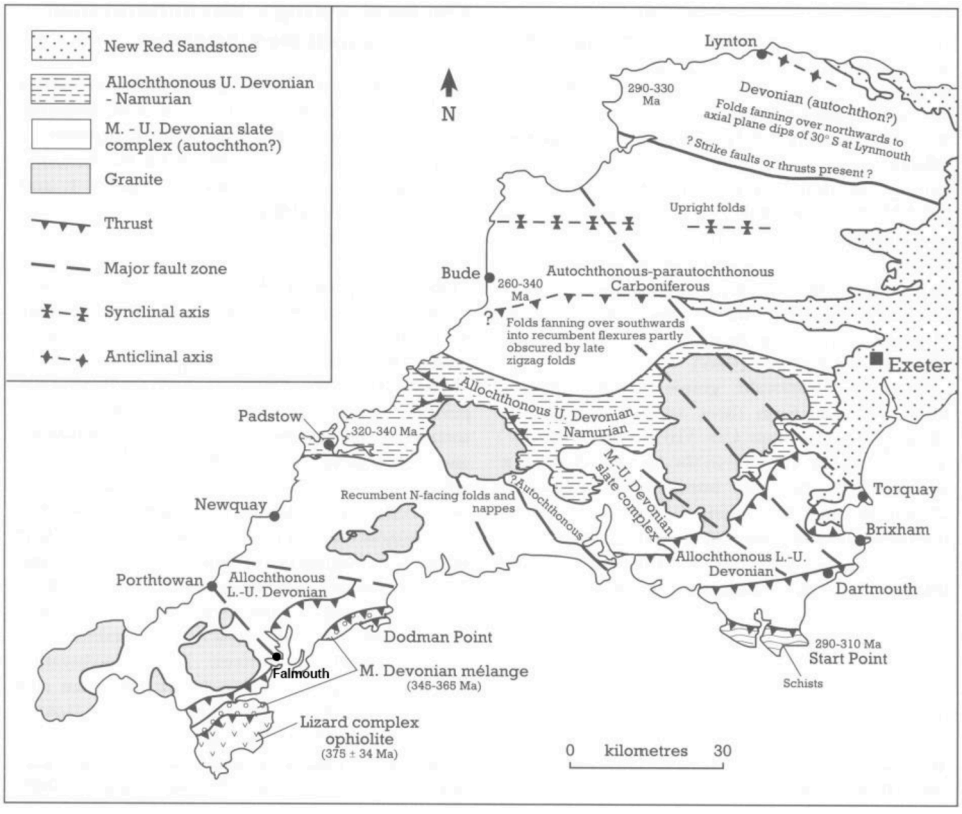

Fig. 1. Map of southwest England showing major structural features, including the large NW-SE striking Porthtowan Fault (PTF) traversing Cornwall (Dineley, 1986).

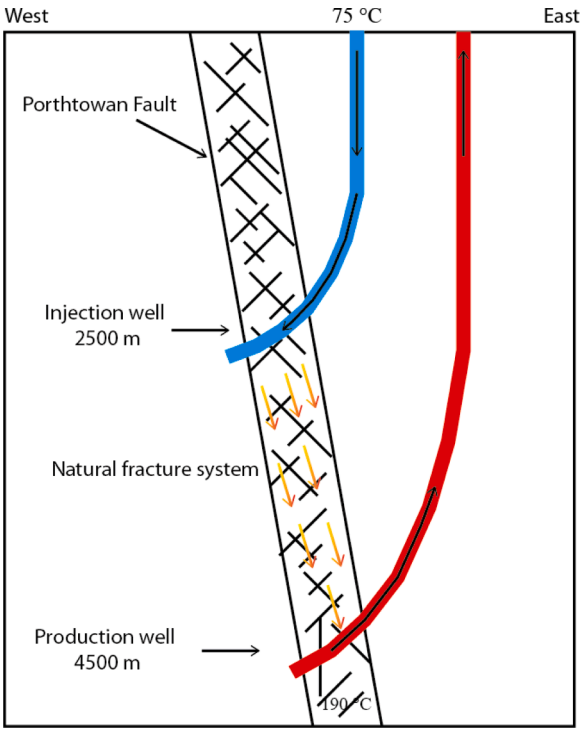

Fig. 2. Schematic presentation of the UDDGP project concept; cross-strike section through the Porthtowan Fault.

address problems of fault instability in geothermal reservoirs (Taron and Elsworth, 2009). Porosity and permeability of both fracture and matrix evolve in response to induced deformation, as conditioned by various constitutive laws. The response of fault permeability and induced seismicity are investigated by examining the evolution of permeability and reactivation slip distance. Distributed flow rates and corresponding enthalpy quantify the performance of the heat energy extraction system.

In this modeling study, the fault-hosted reservoir is characterized in pseudo 3D plane strain condition (Fig. 3) to include the transmissive fault flanked by low permeability host rocks (1500 $m \times 4000\ m \times 15$ m).

The prescribed Porthtowan fault dips at 80° below the horizontal, is 300 m in width and embedded inside the low permeability host granite. The spatial architecture of the fault comprises a low permeability core (30 m) consisting of fine granular gouge ($k \sim 10^{-16}$ m^2) sandwiched between more permeable fault damage zones (270 m) containing extensive joints/fractures resulting from cumulative shear deformation across the fault ($k \sim 10^{-13}$ m^2) (Ledingham et al., 2019). the flow boundary conditions for the all boundaries are set as no-flow type, as the fault rocks are surrounded by the low permeability host granite. It is assumed the fault is bounded by impermeable bedrock and caprock, to prevent fluid leak off from the fault conduits. The boundary conditions and permeability structure are defined to evaluate the effects of pressurization inside fault in triggering instability. It can be expected the open boundaries allow fluid dissipation and delay the onset of fault reactivation. The bottom and left boundaries are set as roller condition with zero normal displacement. Previous characterizations of the Rosemanowes HDR project in Cornwall indicate a bottom hole temperature of ~190 °C at 4500 m, corresponding to a thermal gradient of 0.0375 °C/m. The bottom hole pressure is defined at 53.5 MPa with a pressure gradient of 9.8×10^3 Pa/m and a vertical stress gradient set at 2.648×10^4 Pa/m, the horizontal stress gradients are set at 1.583×10^4 Pa/m and 2.037×10^4 Pa/m (Batchelor, 1979; 1982). The constitutive law representing the elastic-plastic transition of the fault is represented by a ubiquitous joint model, assuming slip-weakening behavior with the shear strength linearly decreasing with the onset of plastic shear strain (Rutqvist et al., 2002; Q. Gan and Elsworth, 2014).

Table 1 summarizes the assumed initial properties for the host rock, fault core and fault damage zones. The bulk moduli for the fault blocks and host rock are 10 GPa and 15 GPa, representing softening due to the presence of fractures. The reduction in elastic properties and friction angle highlights the release of seismic energy through the fault reactivation.

Slip response within the fault is represented by the brittle Mohr-Coulomb failure criterion model, which invokes fault slip weakening law as a necessary condition for inducing fault instability. Brittle behavior defines a single peak strength that subsequently reduces with each increment of plastic strain. The timing of reactivation is determined by the effective stress state and peak friction strength. In this work, the instability of the fault is represented by a ubiquitous joint model in FLAC^{3D} which defines the presence of planes of weakness by the dipping

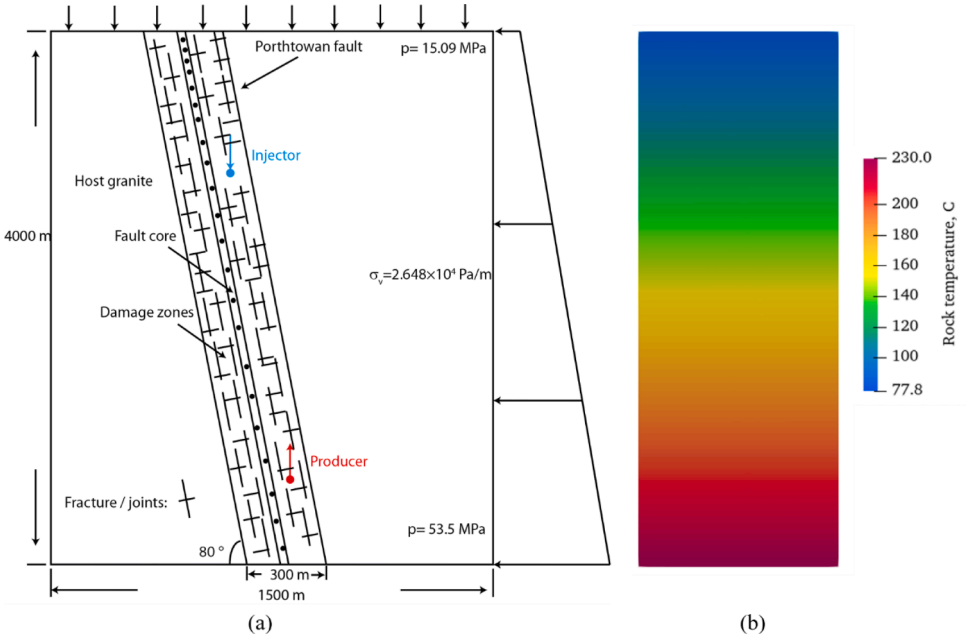

Fig. 3. (a) Schematic of reservoir geometry with prescribed fault architecture, (b) initial distribution of rock temperature (Ledingham et al., 2019).

Table 1
Material properties used in the simulations (Ledingham et al., 2019; Rutqvist et al., 2015).

Parameters	Host rock	Fault damage zone	Fault core
Matrix permeability, m^2	10^{-16}	10^{-15}	10^{-16}
Fracture permeability, m^2	–	2.5×10^{-13}	2.0×10^{-16}
Fracture spacing, m	–	0.5	7
Bulk modulus, GPa	15	10	10
Cohesion, MPa	3	3	3
Matrix porosity	0.1	0.3	0.01
Fracture porosity	0.3	0.3	0.3
Matrix friction angle, deg	45	45	45
Tensile strength, MPa	30	4	4
Poisson's ratio	0.22	0.22	0.22
Joint cohesion, MPa	–	0	0
Joint friction angle, deg	–	28	28
Residual friction angle, deg	–	9	9
Residual plastic strain	–	10^{-3}	10^{-3}
Rock density, kg/m^3	2700	2700	2700
Dilation angle, degrees	0	5	5
Non-linear stiffness, η	–	0.218	0.218
Residual aperture, m	–	2.0×10^{-4}	4.2×10^{-5}
Maximum aperture, m		9.0×10^{-4}	2.018×10^{-4}

angle and strike orientation. The plane of weakness is highlighted by low modulus and strength values (Table 1). This model implements a bi-linear joint-matrix definition to capture the shear/tensile failure that occurs in both joints and matrix with different strengths. The initial static friction angle of fractures is assumed to be 28° The strong cohesion strength allows an initial stable state, and sustained under high stress loading. The friction strength drop from peak to residual friction coefficient aims to create higher strain energy release from fault reactivation (Rutqvist et al., 2015).

3.1. Fault permeability

The evolution of fault permeability is represented by specifying the architecture of the fracture network, including the magnitude of fracture aperture and spacing in the fault-normal and fault-parallel directions. The fracture networks are defined using the MINC (Multiple Interacting Continua) approach in TOUGHREACH with the dual permeability and porosity values for fault core, damage zone and host rock. The permeability of fractures in the fault zone is characterized by a parallel-plate model as (Snow, 1969),

$$k = \frac{b^3}{12s} \tag{1}$$

where b is fracture aperture, and s is the spacing of fractures in each principal direction. The constitutive model for predicting the evolution of aperture is governed by the fracture stiffness and effective stress, given as (Min et al., 2009),

$$b_s = b_r + (b_{max} - b_r)\exp\left(-\eta\left(\sigma' - \sigma_0'\right)\right) \tag{2}$$

where b_r represents the residual aperture (m), b_{max} is the maximum aperture at zero stress level (m), η is the non-linear fracture stiffness (1/MPa), σ' is the effective stress, σ_0' is effective stress at which zero deformation occurs (usually zero). The shear displacement of fractures u_{js} increases normal aperture b_{dila} by dilation according to,

$$b_{dila} = u_{js}\tan\psi_{jd} \tag{3}$$

The local plastic shear strain increment for shear failure along a weak fault plane $\Delta\varepsilon^{P_s}_{3'3'}$ is calculated as

$$u_{js} = \Delta\varepsilon^{P_s}_{3'3'} * s$$

$$\Delta\varepsilon^{P_s}_{3'3'} = \lambda^s \tan\psi_{jd} \tag{4}$$

$$\lambda^s = \frac{\tau^0 + \sigma^0_{3'3'}\tan\phi_j - c_j}{2G + \alpha_1 \tan\psi_{jd}\tan\phi_j} \tag{5}$$

where λ^s is the associated plastic shear for the solid element, ψ_{jd} is the dilation angle of the fracture, G is shear modulus, ϕ_j is joint friction angle, c_j is joint cohesion, $\sigma_{3'3'}$ is the normal traction component on the plane of weakness, and the superscript 0 indicates the values obtained before detection of failure on this plane.

Thus, the final lumped expression for calculating the permeability of fractures is given as

$$k = \frac{b^3}{12s} = \frac{(b_s + b_{dila})^3}{12s} \tag{6}$$

3.2. Well configuration and injection schedule

The currently drilled geothermal system placed an injection well at shallow depth (2500 m) with the production well tapping the fault at greater depth (4500 m). Our modeling study explores the influence of well configuration by switching the location of injector and producer (top-to-bottom to bottom-to-top). In order to obtain economic recovery from this conceptual design, the fluid circulation rate must be ~20–60 *l/s*. Consequently, it is critical to examine the influence of well configuration in altering the stress state on the fault and its impact on the long-term performance for energy production.

When the injector is switched at the 4500 m depth, high constant injection rates (~20 kg/s) lead to excessive large bottom hole pressure ramp-up and early seismic events, which actually causes instability of code. Therefore, a maximum injection rate is implemented at 17 kg/s. Table 2 summarizes the numerical modeling schedule for different well configurations with different injection rates and bottom hole pressures. Cases A - C are designed to examine the influence of different production pressures in controlling the fluid circulation rate along the fault. Cases D - F compare different well configurations by swapping the locations of injector and producer. Together, these cases provide illuminating results in predicting the evolution of permeability structure, and also define the well configuration anticipated to deliver the best performance with respect to maximizing power generation and minimizing the potential for induced seismicity.

4. Results and discussion

The prescribed scenarios of Table 2 explore the influence of injection–production configuration and schedule, given the assumed frictional failure model, on the evolution of geothermal energy recovery and induced seismicity in time and space. Cases A – C highlight the influence of bottom hole pressure (BHP) variation in modifying fault behavior, and Cases D - F explore the influence of injector-producer locations and variable circulation rates along fault.

The evolution of pressure along the fault dip is determined by injectate balance between the injector and producer wells. Fig. 4 shows the pore pressure distribution at 10^8s (~3.17 y) and an increase in pore pressure for a high production pressure (BHP) of 25 MPa (Case A). The lower production pressure for Cases B (20 MPa) and C (15 MPa) shows lower formation pressures with larger fluid circulation rates. Compared

Table 2
Comparison of various well configurations and injection schedules.

Scenario	Well pattern	Injection rate (kg/s)	Production (BHP)
Case A	Top injection	17	25 MPa
B	Top injection	17	20 MPa
C	Top injection	17	15 MPa
D	Bottom injection	17	20 MPa
E	Bottom injection	13	20 MPa
F	Bottom injection	10	20 MPa

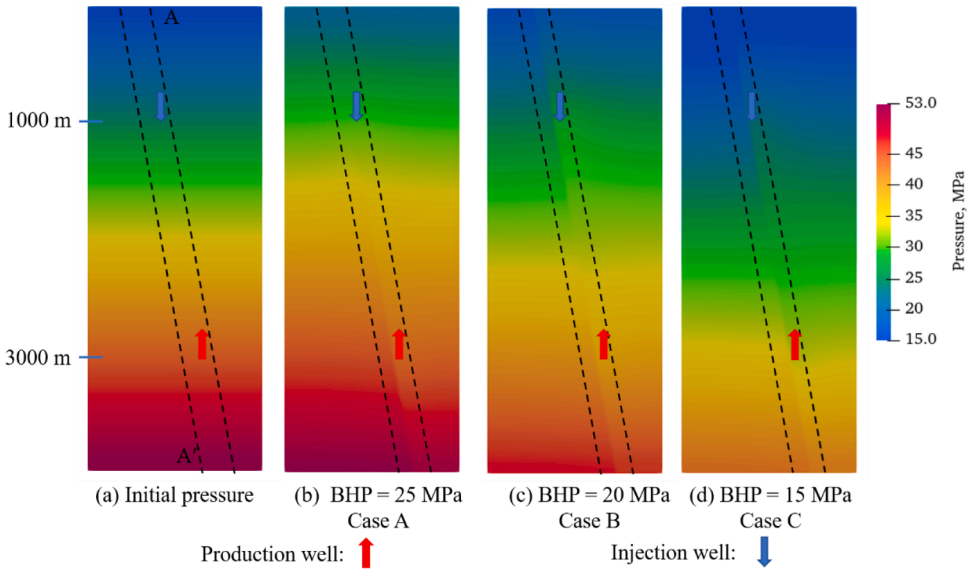

Fig. 4. Pressure distributions relative to the initial condition (a) for different BHP in bottom production well (b-d) after injection and production for 10^8 s (~3.17y).

to the initial pore pressure distribution, the pressure inside the fault zone for Case B and C decreased around 5 MPa and 9.6 MPa due to depletion, while the pressure level in Case A increased ~5 MPa over the initial magnitude. The average production rates before 10^6s for Cases A-D are 16, 18, 22, and 12 kg/s. The lowered pressure gradient facilitates fluid flow downward to the production well by enhancing fluid velocity. The variation of fluid residence time inside fault channels directly affects heat transfer between the injected fluid and the hot host rocks.

Fig. 5 shows the pore pressure distribution for different bottom injection rates at 2.5×10^6 s (~30d). High pore pressure is required to overcome the resistance from gravity and hydro–static stress. This excessively high pressure also increases the potential for fault reactivation (seismicity). Assuming Darcian flow along the fault with initial permeability at 2.5×10^{-13} m^2, the average fluid velocity v along the fault strike for Cases D-F are calculated at 8.4×10^{-4}, 1.25×10^{-4}, and 6.2×10^{-5} by using,

$$v = \frac{k}{\mu}\frac{dP}{dL} \tag{7}$$

The slow fluid migration velocity is expected to reduce the efficiency of thermal energy extraction. Given the dramatically different pressure evolution for the different injection -production scenarios, it is critical to examine the associated evolution of temperature.

Figs. 6 and 7 show temperature distributions for Cases A - C at 10^8 s (~3.17y), and Case D - F at 2.5×10^6 s (~30d). The temperature distributions for down-dip and up-dip are compared separately owing to

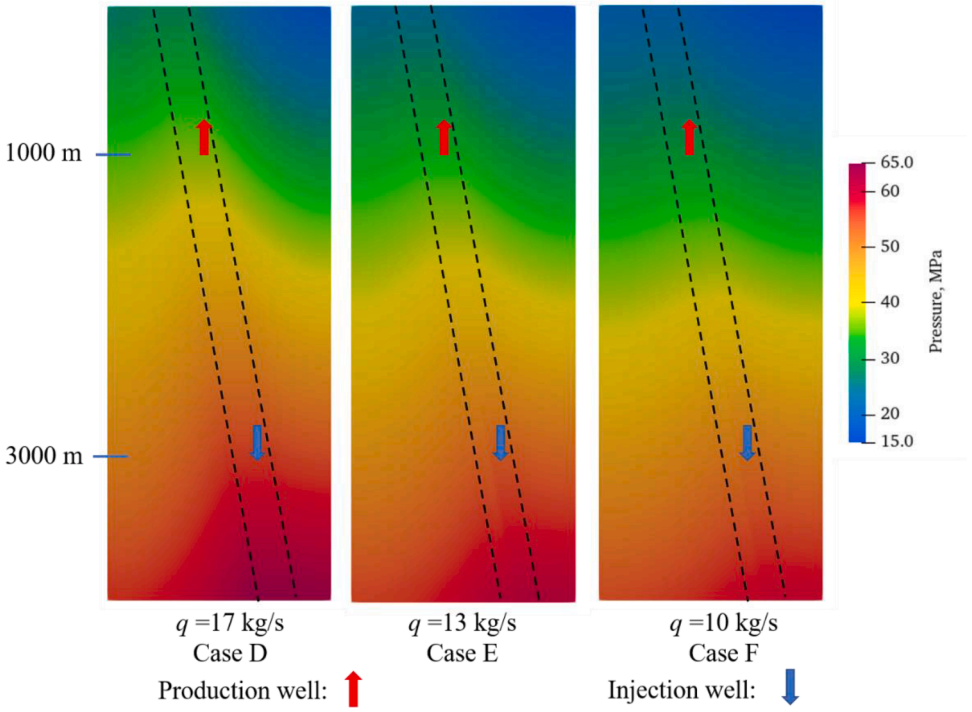

Fig. 5. Pressure distributions for different injection rates (17 kg/s Cases D, 13 kg/s in Case E, and 10 kg/s Case F) at 4500 m depth, after injection and production for 2.5×10^6 s (~30d).

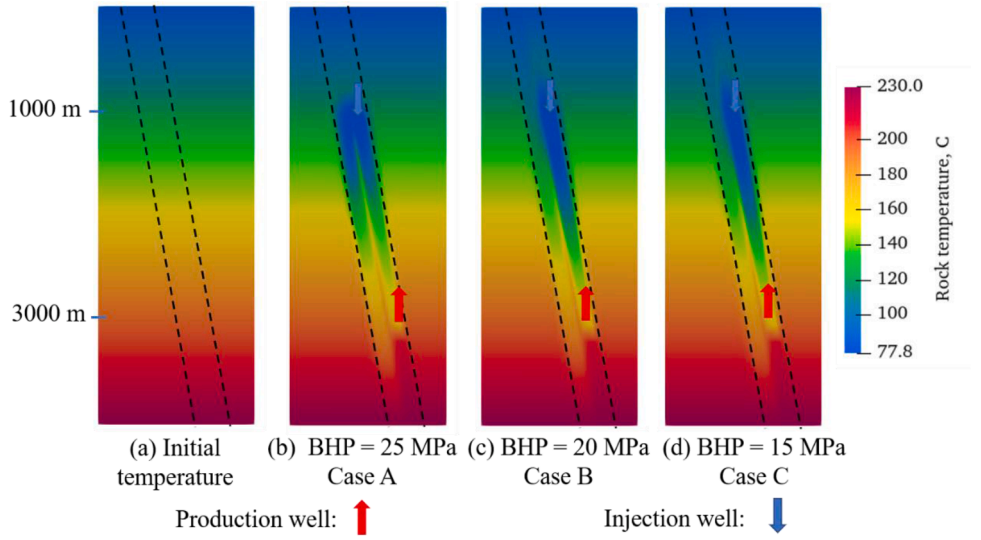

Fig. 6. Temperature distributions for the initial condition (a) and Case A (b), Case B (c), and Case C (d) after injection and production for 10^8 s (~3.17y).

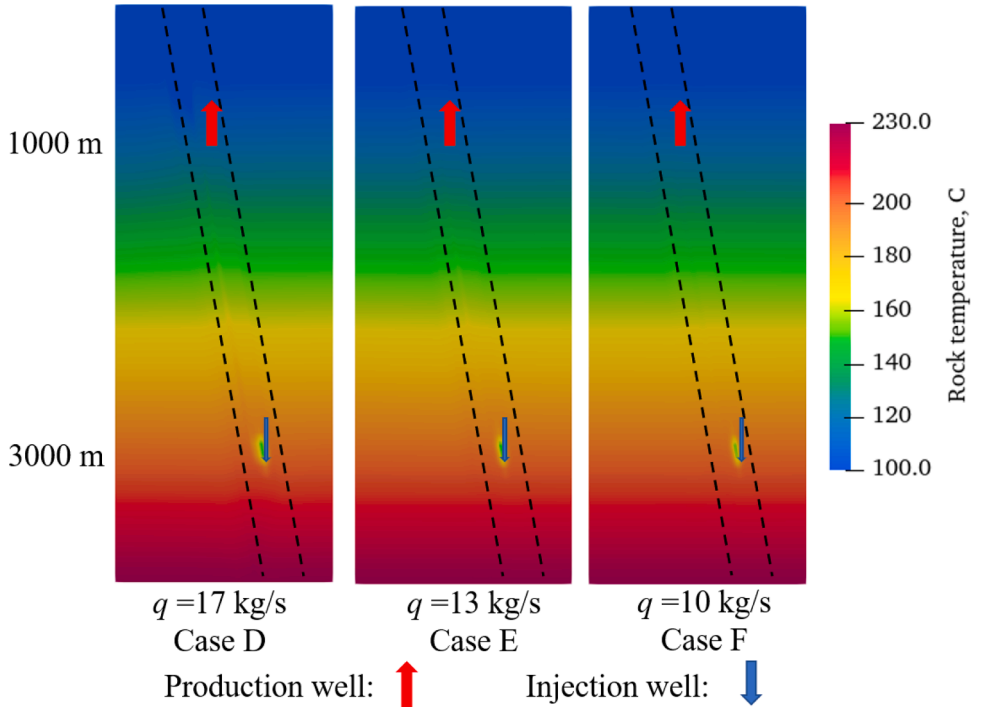

Fig. 7. Temperature distributions for Cases D, E, and F after injection and production for 2.5×10^6 s (~30d).

the different time-evolution of fault permeability. The major difference in temperature among the top injection configurations is the cooling of both footwall and hanging wall in Case A (BHP=25 MPa) versus cooling limited to the hanging wall in Case B (BHP=20 MPa) and C (BHP=15 MPa). The difference results from over-pressurization and associated plastic deformation at shallow depth around the injector in Case A, which enhances permeability in both the fault damage zone and the fault core. The fault seal is breached, leading to penetration of fluids into the footwall. Consequently, there is strong cooling within the footwall in Case A, and less thermal drawdown in Cases B & C due to lower pore pressure. In the reversed injection scenarios (bottom to top) of Case D - F (Fig. 7), t cooling is localized around the injector, where temperature decreases by ~40 °C after only 1-month of injection. The fluid absorbs heat while migrating to the production well at shallow depth.

The architecture of fault permeability is critical in determining fluid pathways and associated heat transfer modes. Fig. 8(a) shows the initial fault permeability structure, comprising a low permeability fault core bracketed by permeable damage zones with extensive joints. The fault core prevents direct fluid communication between footwall and hanging wall, effectively sealing the fault. The gradual fluid mass accumulation in the shallow depth also assist in the plastic deformation by reducing the effective stress state, as the high permeability enhancement is identified in hanging wall (Fig. 9).

Fig. 8(d) shows an order-of-magnitude permeability enhancement at shallow depth in Case A for a BHP of 25 MPa at the production well, while no significant permeability evolution occurs in Cases B & C. In Case A, we identify simultaneous permeability enhancement in the fault core, which breaches the fault seal. The permeability field for Case A controls and contributes to the rock temperature distribution shown in Fig. 7(a). Enhanced transverse permeability at shallow depth allows

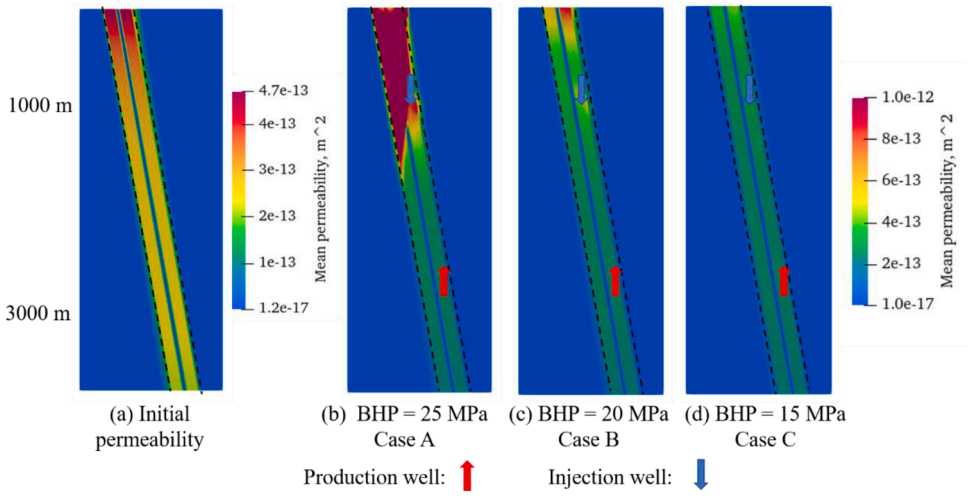

Fig. 8. Spatial distributions of permeability for the initial condition (a) relative to Cases A (b), B (c), and C (d) after injection and production for 10^8 s (~3.2y).

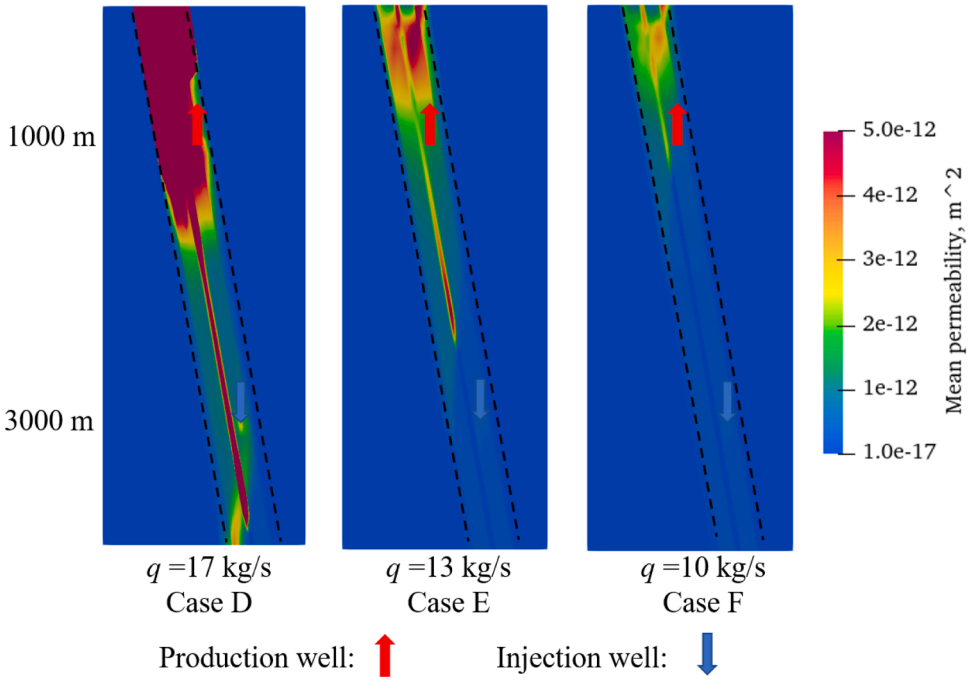

Fig. 9. Spatial distributions of permeability for Cases D, E, and F after injection and production for 2.5×10^6 s (~30d).

fluid to penetrate horizontally, with cold fluid migrating to the footwall and absorbing heat.

The permeability evolution for bottom injection is dramatically different from that for top injection. Fig. 9 presents the spatial permeability distribution for Cases D - F at 2.5×10^6 s (~30d). Given the almost same fluid extraction configuration, the highest injection rate of 17 kg/s in Case D leads to highest fluid accumulation and pressure build-up near producer at shallow depth (Fig. 5), which generates large permeability enhancement in the top of the fault at shallow depth in Case D. The induced shear dilation that results from extensive plastic failure prompts the opening of the initially tight fault core. Fault core permeability is enhanced by more than five orders of magnitude, to 5×10^{-12} m^2 in Case D.

The volumetric strain distribution illustrates the influence of thermal depletion in modifying the stress state over the entire fault segment. The variation of bottom hole pressure determines the velocity of fluid circulation from injection well to production well, decrease from 8.4×10^{-4} m/s in Case D to 6.2×10^{-5} m/s in Case F. A BHP of 25 MPa for withdrawal in Case A allows fluid mass to accumulate at shallow depth. The volumetric strain at 10^8 s (~3.17y) in Fig. 10(a) indicates strong compaction from injector to producer, due to the comingled influences of pressurization and thermal depletion. Cases D - F show the volumetric strain distribution at time 2.5×10^6 s (~30d), predominantly as a result of hydro-mechanical deformation. Pressurization expands along the fault damage zones, with the magnitude of induced strain decreasing with depth, due to the stronger impact of compaction. Thermal drawdown exerts significant influence in relieving and unloading the fault stress state (Gan and Lei, 2020).

Fig. 11 shows the spatial distribution of effective normal stress, shear stress, and Coulomb stress change along fault dip for the fault damage zone and core zone separately. As the fault core and damage zone are defined with different hydraulic properties (Table 1), the pressurization and cooling leads to different levels of fault reactivation, due to the coupled influence of poroelastic stress changes, thermoelastic stress

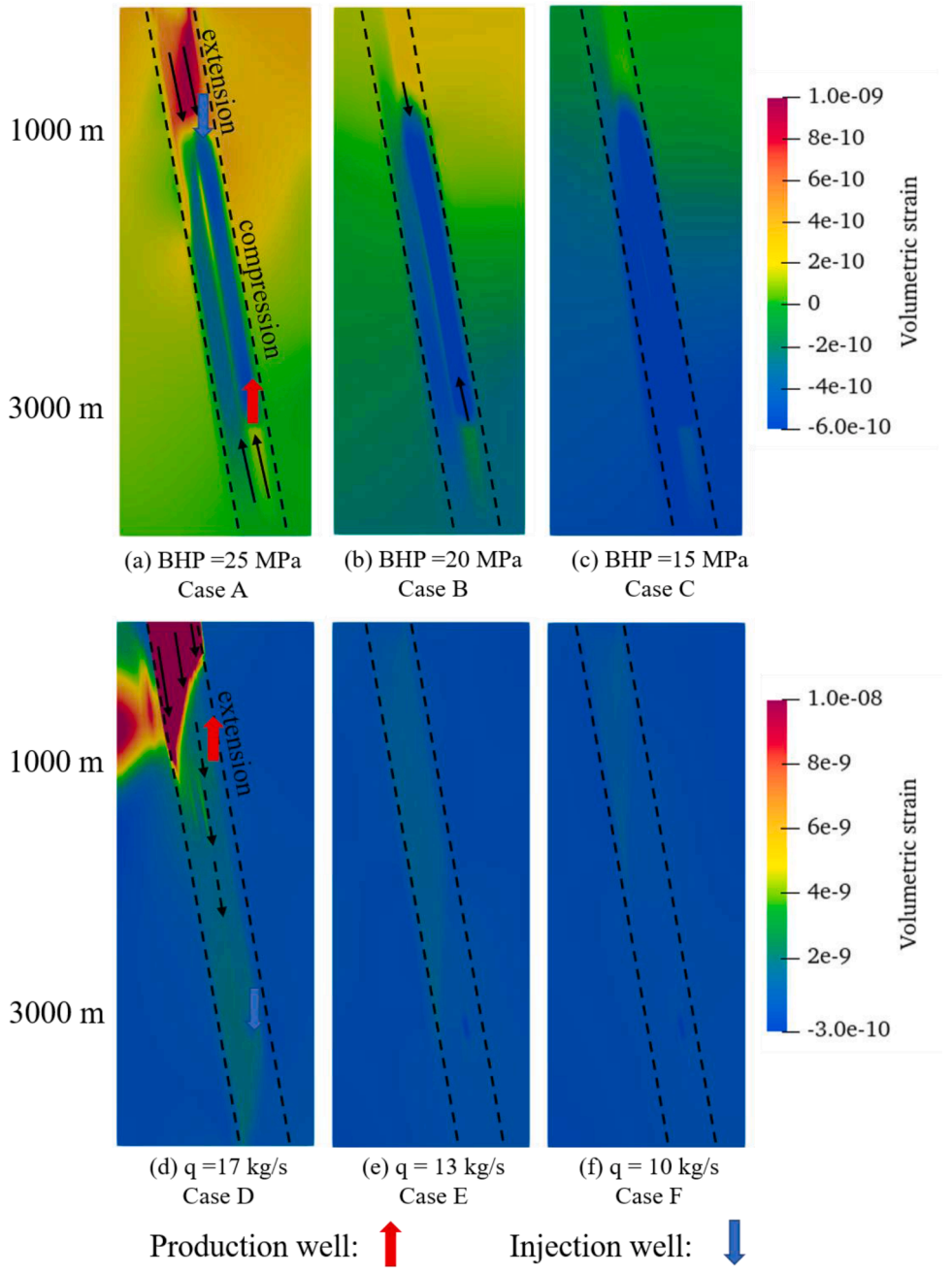

Fig. 10. Comparison of volumetric strain distributions for Cases A-C (a-c) after 10^8 s (~3.2y) and Cases D - F (d-f) after 2.5×10^6 s (~30d).

changes, and pore pressure diffusion. The Coulomb stress change $\Delta\tau_{cs}$ is defined as.

$$\Delta\tau_{cs} = \Delta\tau_s - \mu\Delta\sigma_n + \mu\Delta P \tag{8}$$

where $\Delta\tau_s$ is the change in shear stress, μ is the friction coefficient, $\Delta\sigma_n$ is the change in normal stress, and ΔP denotes the pore pressure change in the fault. The thermal unloading (cooling) affects the effective normal stress distribution along the path between the two wells, especially adjacent to the injector, which is subject to the strongest cooling. The effective normal stress around the producer in Case A-C also reflects a reduction of effective normal stress. Positive Coulomb stress changes indicate an unstable stress path along the fault, whereas negative Coulomb stress changes represent stabilization. The fault core has a slightly higher effective normal stress than the damage zone due to slower pressurization. In Case A, the shear stress drop in the fault damage zones from the injector to the deep 3000 m depth is higher than that in the fault core . However, the shear stress drops in the fault core at shallow depth (100 m – 1000 m) for Cases A and D are greater than those in the fault damage zone, which indicates stronger fault reactivation in the fault core at shallow depth. The Coulomb stress changes in Fig. 11e-f demonstrate that the fault in Cases B and C remains very stable. In Case A the fault core at the 100 m – 1000 m depth displays larger positive Coulomb stress changes than the fault INCdamage zone at the same depth. The fault instability in Case A focuses at a depth of 100 m – 2000 m. Up-dip circulation with the bottom injection scenario of Case D results in a destabilizing stress path for the entire fault.

The seismic energy released through each shear slip event may be quantified by the event moment M_0, with the corresponding moment magnitude M_s calculated as the defined $M_s - M_0$ relationship (Hanks and Kanamori, 1979),

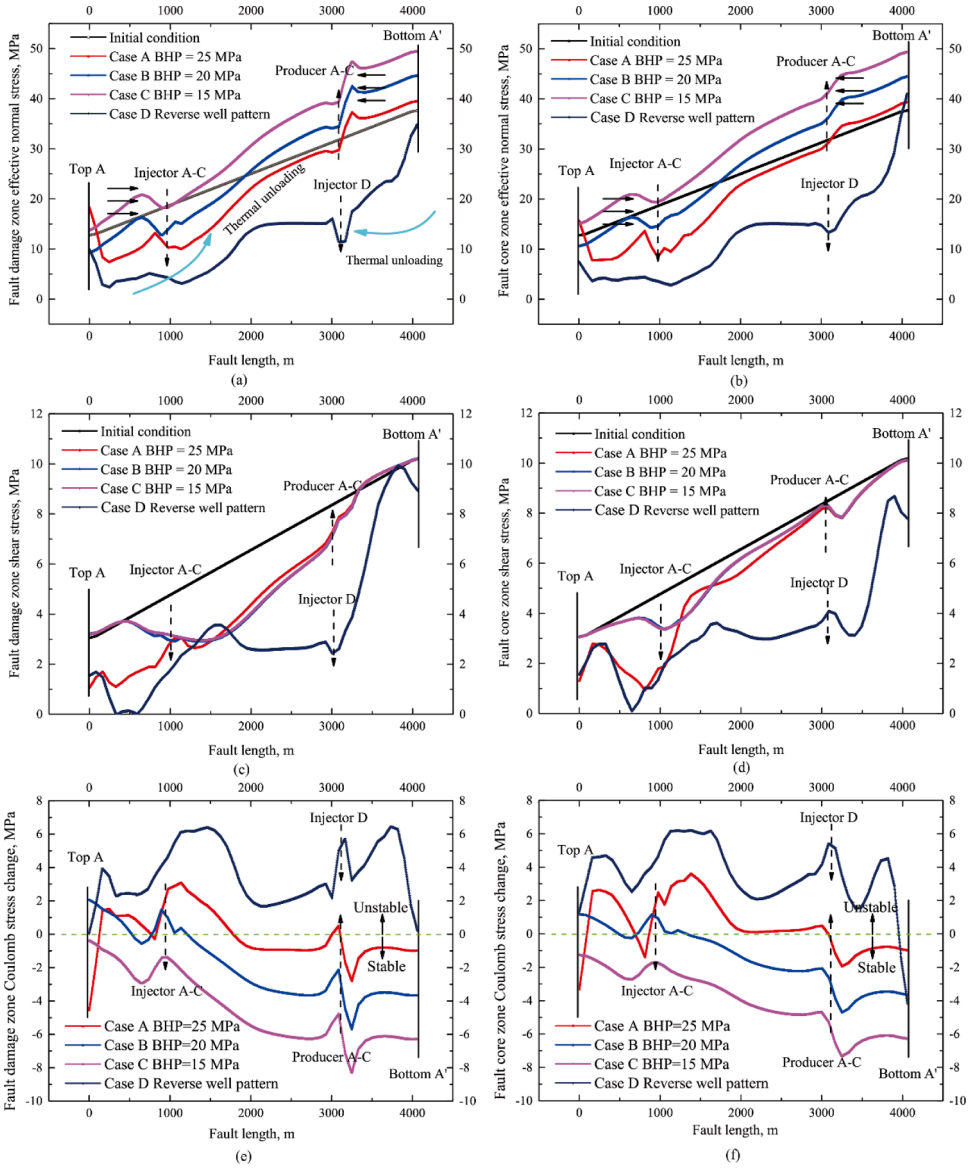

Fig. 11. Distribution of effective normal stress (a-b), shear stress (c-d), Coulomb stress change within the damage zone (e) and core zone (f) along the dip of the fault.

$$M_s = \frac{2}{3}\log M_0 - 10.7 \tag{9}$$

$$M_0 = G{\cdot}d{\cdot}A \tag{10}$$

where G is the shear modulus, d is slip displacement, and A is the rupture area. The validity of estimating induced seismicity using the shear strain in FLAC^{3D} has been explored and benchmarked (Wassing et al., 2014). Each seismic event from an individual faulted numerical cell is recorded by measuring the joint plastic shear strain. The limitation of this approach is the potential sensitivity to element mesh size. There is an intrinsic balance between the number of slip events and magnitude of event. A coarse mesh will reduce the total number of fault elements, but reduce the resultant plastic shear strain, due to lack of high resolution for the sliding elements . The lack of fine-rupture propagation for small timesteps comes from the nature of continuum simulator. Discrete element models have the advantages in shaping dynamic rupture propagation decay due to the frictional strength evolution from velocity weakening or strengthening mechanism. The advantage of our approach here is to characterize the propagation of rupture through a cloud of events under a brittle failure assumption. The dynamic propagation of rupture area at each timestep can be revealed by examining the spatial and temporal distribution of induced seismic events. The purpose is to characterize the location of seismic events in space and time . Fig. 12 selects Cases A and D to explore the resulting seismic events in terms of locations, magnitudes, and cumulative event numbers. The induced seismic events in Case A initiate from the top of the formation, which is prone to failure due to the low effective stress state. The cloud of seismic events is localized around the injector. The maximum magnitude M_s is 2. The final cumulative number of events is ~30,000.

Switching to bottom injection slightly delays the onset of events, due to slow propagation of the hydraulic and thermal fronts to the critically stressed zones. However, the significant elevation of pore pressure increases the extent of the ruptured area and the total number of events. The magnitude of seismic events continuously increases for constant injection rate. Seismic rupture also propagates downward. Comparison between the two scenarios indicates that the vicinity of the production well remains relatively quiet and stable in the Case A. Continuous production essentially maintains the stress state below a critical level (Fig. 11). The fault is seismic event free for Cases B & C.

It is also critical to examine the performance of thermal energy recovery from the fault. The magnitude of instantaneous electric power

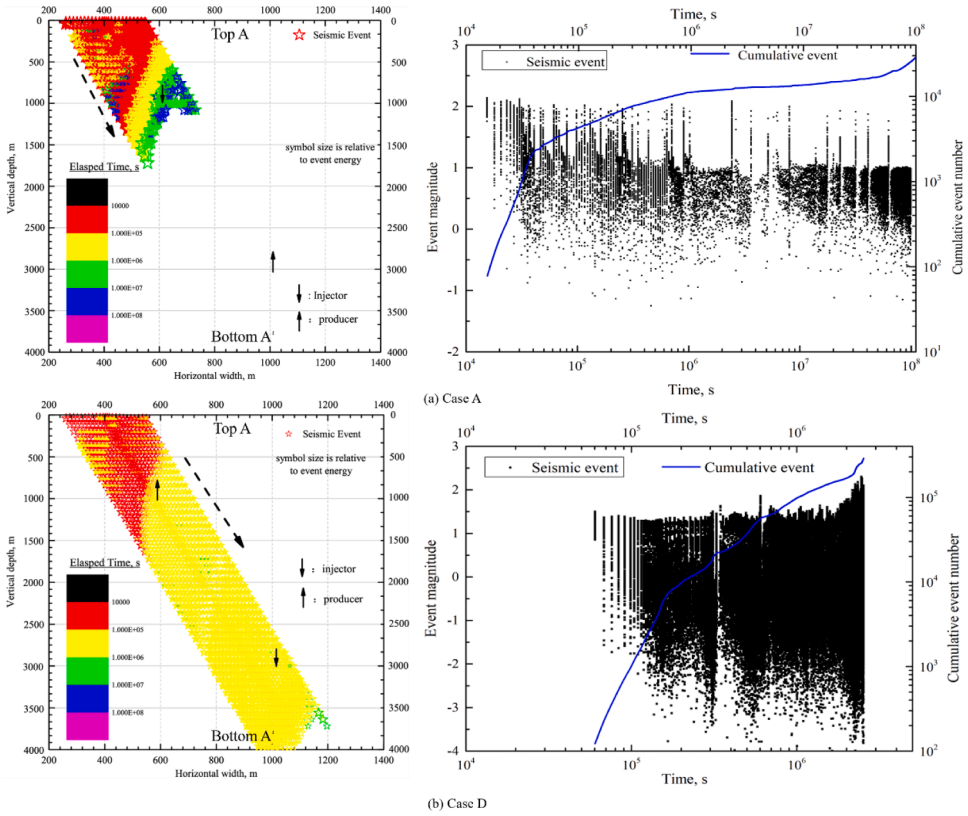

Fig. 12. Spatial and temporal distribution of induced seismic events. Spatial distribution (left side) for Cases A and D, with symbol size proportional to event magnitude. Daily event magnitudes & cumulative number of events (right side) for Cases A and D.

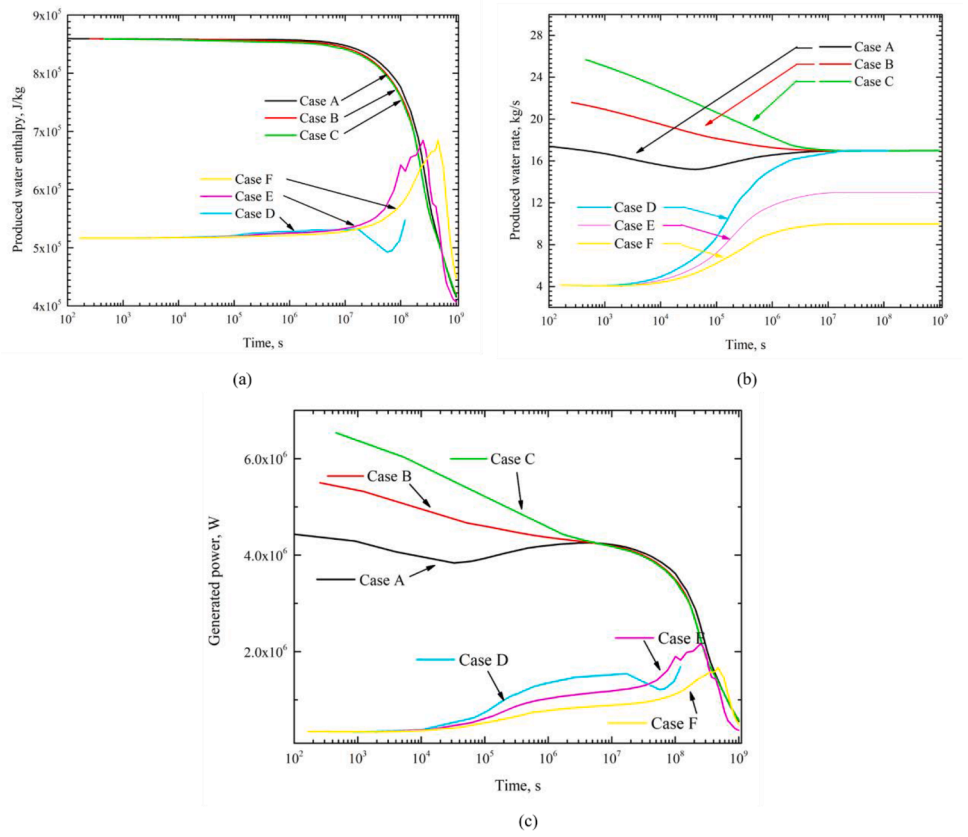

Fig. 13. Evolution of produced water enthalpy (a), mass flow rate at the production well (b), and associated power (c) recovered from the reservoir over 10^9s (31.7*y*) for Cases A-F.

generation W_h is calculated as a product of flow rate and the enthalpy of the produced water as (*Pruess*, 2006),

$$W_h = \alpha q_{pro}(h_{pro} - h_{inj}) \quad (11)$$

where α is the heat utilization efficiency, assumed to be 0.5 in this calculation (*Sanyal and Butler*, 2005), h_{pro} is the water enthalpy at the production well, h_{inj} is the enthalpy of the injected cold water, which is equal to $3.5 \times 10^5 j/kg$ and q_{pro} is the flow rate in the production well (kg/s).

Fig. 13 shows the evolution of water enthalpy (a), flow rate (b), and generated power magnitude (c) over the duration of the simulation (10^9s or31.7y). The instantaneously generated power magnitude is calculated based on Eq. (11) and presented in Fig. 13(c). Case C in the down-dip circulation scenario return the highest cumulative power generation, primarily due to the high flow rate in the production well operating at 15 MPa bottom hole pressure. The final production rate levels off at the injection rate of 17 kg/s Production wells located at greater depth also help to ensure that produced water is maintained at a higher enthalpy ($\sim 5.0 \times 10^5 J/kg$), while locating the production well at shallower depth leads to loss of enthalpy during transport along the fault. Switching the well pattern to bottom injection leads to a gradual increase in the enthalpy of water at the production well. The flow rate in the production well also increases at early times, partly as a result of permeability enhancement along dip. However, given the potential hazards arising from the induced seismic events that enhance permeability, the switching of the well configuration will not be favorable for either increasing production or reducing seismicity. There is enthalpy drawdown in produced water from 10y. The lower production pressure in the down-dip circulation design is necessary to prevent pressure build-up inside the fault and trigger fault instability, especially at shallow depth, while maintaining the cumulative power generation at higher level.

5. Conclusions

This work examined well configurations tapping a sub-vertical fault with regard to efficiency of heat transfer and mitigating induced seismicity. We used a coupled Thermal-Hydraulic-Mechanical model, based on the flow and stimulation geometry of the currently ongoing United Downs Deep Geothermal Power (UDDGP) project. Both economic feasibility and induced seismicity are taken into consideration. We examine the consequences of injecting top to bottom within the fault, as currently planned, and then the converse bottom to top injection scenario.

The results for top injection – bottom production suggest that shear deformation is likely to occur first in the critically-stressed shallow reservoir. The fault seal may be breached due to significantly enhanced permeability of the fault core. Cold fluid injected inside the fault zone may penetrate transversely and simultaneously increase the area of heat transfer. The thermal drawdown arising from fluid circulation between wells along the dip direction substantially relieves the fault stress state by unloading, thereby enhancing connectivity within the fault. The mechanism causing initial fault instability at shallow depths is primarily direct pressurization. Thermal cooling influences rupture propagation from the localized injector zone to ~2000 m depth. Switching the location of injection and production wells impedes fluid circulation because of the buoyancy and lithostatic stress gradient. High injection pressure is required for up-dip circulation. Furthermore, the fluid loses enthalpy into the lower-temperature host rock at shallow depth. Consequently, switching well locations will not enhance the expected efficiency of heat energy extraction. To the contrary, the flow rate and enthalpy of the produced water will both be reduced.

Shallow injection with BHP at 25 MPa (Case A) could trigger ~30,000 seismic events over the duration of the simulation (~30y), mainly due to pressurization at shallow depth. There are few seismic events with shallow injection at lower bottom hole pressures (Cases B and C), which also allows more fluid to be produced from the fault zone. Seismic rupture initiates at shallow depth and propagates toward the injector, while the deep formation remains relatively seismically quiescent. Switching injection to the bottom location dramatically increases the total number and magnitude of seismic events and therefore is not favorable for a sustainable production of geothermal energy.

CRediT author statement

The author Quan Gan would like to take the opportunity to thanks all the authors in this work, providing their help and contributions to the published work.

Quan Gan: Model development, data analysis, and writing original draft, and revision.

Zijun Feng: Conceptualization, and partial funding support;

Honglian Li: model set-up and paper review

Jun Liu: data collection and address paper review

Lei Zhou: model set-up, data collection, and paper review

Derek Elsworth: conceptualization, data formal analysis, paper review, software resource.

Declaration of Competing Interest

All persons who meet authorship criteria are listed as authors, and all authors certify that they have participated sufficiently in the work to take public responsibility for the content, including participation in the concept, design, analysis, writing, and manuscript revision process. Furthermore, each author certify that this material or similar material has not been and will not be submitted to or published in any other publications.

Acknowledgement

This work was partly supported by the Key Laboratory of In-situ Property-improving Mining of Ministry of Education, Taiyuan University of Technology, the National Natural Science Foundation of China (51774056), and the Science and Technology Department of Sichuan Province (Grant No. 21YFH0048).

Supplementary materials

Supplementary material associated with this article can be found, in the online version, at doi:10.1016/j.geothermics.2021.102204.

References

Anyim, K., Gan, Q., 2020. Fault zone exploitation in geothermal reservoirs: production optimization, permeability evolution and induced seismicity. Adv. Geo-Energy Research 4 (1), 1–12.
Batchelor, A.S., Pearson, C.M., 1979. Preliminary studies of dry rock geothermal exploitation in south-west England. Inst. Mining Metallurgy Translat. 88, B51–B56.
Cappa, F., Rutqvist, J., 2012. Seismic rupture and ground accelerations induced by CO2 injection in the shallow crust. Geophys. J. Int. 190 (3), 1784–1789.
Donnelly, L.J., 2006. A review of coal mining induced fault reactivation in Great Britain. Q. J. Eng. Geol. Hydrogeol. 39 (1), 5–50.
Dineley, D.L., 1986. Cornubian quarter-century; advances in the geology of south-west England, 1960-1985. Proc. Ussher Society 6 (3), 275–290.
Ellsworth, W.L., 2013. Injection-induced earthquakes. Science 341 (6142).
Fang, Y., Wang, C., Elsworth, D., Ishibashi, T., 2017. Seismicity-permeability coupling in the behavior of gas shales, CO 2 storage and deep geothermal energy. Geomecha. Geophys. Geo-Energy Geo-Res. 3 (2), 189–198.
Fang, Y., Elsworth, D., Ishibashi, T., Zhang, F., 2018. Permeability evolution and frictional stability of fabricated fractures with specified roughness. J. Geophys. Res. 123 (11), 9355–9375.
Gan, Q., Elsworth, D., 2016a. A continuum model for coupled stress and fluid flow in discrete fracture networks. Geomech. Geophys. Geo-Energy Geo-Res. 2 (1), 43–61.
Gan, Q., Lei, Q., 2020. Induced fault reactivation by thermal perturbation in enhanced geothermal systems. Geothermics 86, 101814.
Gan, Q., Elsworth, D., 2014a. Analysis of fluid injection-induced fault reactivation and seismic slip in geothermal reservoirs. J. Geophys. Res. 119 (4), 3340–3353.

Gan, Q., Elsworth, D., 2014b. Thermal drawdown and late-stage seismic-slip fault reactivation in enhanced geothermal reservoirs. J. Geophys. Res. 119 (12), 8936–8949.
Gan, Q., Elsworth, D., 2016b. Production optimization in fractured geothermal reservoirs by coupled discrete fracture network modeling. Geothermics 62, 131–142.
Gischig, V.S., Giardini, D., Amann, F., Hertrich, M., Krietsch, H., Loew, S., Maurer, H., Villiger, L., Wiemer, S., Bethmann, F., Brixel, B., 2020. Hydraulic stimulation and fluid circulation experiments in underground laboratories: stepping up the scale towards engineered geothermal systems. Geomech. Energy Environ. 24, 100175.
Hanks, T.C., Kanamori, H., 1979. A moment magnitude scale. J. Geophys. Res. 84 (B5), 2348–2350.
Juncu, D., Árnadóttir, T., Geirsson, H., Guðmundsson, G.B., Lund, B., Gunnarsson, G., Hooper, A., Hreinsdóttir, S., Michalczewska, K., 2020. Injection-induced surface deformation and seismicity at the Hellisheidi geothermal field, Iceland. J. Volcanol. Geotherm. Res. 391, 106337.
Kim, K.H., Ree, J.H., Kim, Y., Kim, S., Kang, S.Y., Seo, W., 2018. Assessing whether the 2017 Mw 5.4 Pohang earthquake in South Korea was an induced event. Science 360 (6392), 1007–1009.
Ledingham, P., Cotton, L., Law, R., 2019. The united downs deep geothermal power project. In: Proceedings, 44th Workshop on Geothermal Reservoir Engineering. Stanford, California. Stanford University.
Moeck, I., Bloch, T., Graf, R., Heuberger, S., Kuhn, P., Naef, H., Sonderegger, M., Uhlig, S., Wolfgramm, M., 2015. The St. Gallen project: development of fault controlled geothermal systems in urban areas. In: Proceedings World Geothermal Congress, pp. 1–5.
Min, K.B., Rutqvist, J., Tsang, C.F., Jing, L., 2004. Stress-dependent permeability of fractured rock masses: a numerical study. Int. J. Rock Mech. Min. Sci. 41 (7), 1191–1210.
Min, K.B., Jing, L., 2003. Numerical determination of the equivalent elastic compliance tensor for fractured rock masses using the distinct element method. Int. J. Rock Mech. Min. Sci. 40 (6), 795–816.
Parker, R., 1999. The Rosemanowes HDR project 1983–1991. Geothermics 28 (4–5), 603–615.
Pruess, K., 2006. Enhanced geothermal systems (EGS) using CO_2 as working fluid—A novel approach for generating renewable energy with simultaneous sequestration of carbon. Geothermics 35 (4), 351–367.
Rosberg, J.E., Erlström, M., 2019. Evaluation of the Lund deep geothermal exploration project in the Romeleåsen Fault Zone, South Sweden: a case study. Geothermal Energy 7 (1), 10.
Rinaldi, A.P., Vilarrasa, V., Rutqvist, J., Cappa, F., 2015. Fault reactivation during CO_2 sequestration: effects of well orientation on seismicity and leakage. Greenhouse Gases 5 (5), 645–656.
Rutqvist, J., Wu, Y.-.S., Tsang, C.-.F., Bodvarsson, G., 2002. A modeling approach for analysis of coupled multiphase fluid flow, heat transfer, and deformation in fractured porous rock. Int. J. Rock Mech. Min. Sci. 39, 429–442.
Rutqvist, J., Rinaldi, A.P., Cappa, F., Moridis, G.J., 2015. Modeling of fault activation and seismicity by injection directly into a fault zone associated with hydraulic fracturing of shale-gas reservoirs. J. Pet. Sci. Eng. 127, 377–386.
Ruina, A., 1983. Slip instability and state variable friction laws. J. Geophys. Res. 88 (B12), 10359–10370.
Sanyal, S.K., Butler, S.J., 2005. An analysis of power generation prospects from enhanced geothermal systems. Geothermal Res. Council Trans. 29, 131–138.
Samuelson, J., Elsworth, D., Marone, C., 2009. Shear-induced dilatancy of fluid-saturated faults: experiment and theory. J. Geophys. Res. 114 (B12).
Segall, P., Lu, S., 2015. Injection-induced seismicity: poroelastic and earthquake nucleation effects. J. Geophys. Res. 120 (7), 5082–5103.
Scholz, C.H., 1998. Earthquakes and friction laws. Nature 391 (6662), 37–42.
Snow, D.T., 1969. Anisotropie permeability of fractured media. Water Resour Res 5 (6), 1273–1289.
Taron, J., Elsworth, D., 2009. Thermal–hydrologic–mechanical–chemical processes in the evolution of engineered geothermal reservoirs. Int. J. Rock Mech. Min. Sci. 46 (5), 855–864.
Vilarrasa, V., Rutqvist, J., Rinaldi, A.P., 2015. Thermal and capillary effects on the caprock mechanical stability at In Salah, Algeria. Greenhouse Gases 5 (4), 449–461.
Wiprut, D., Zoback, M.D., 2000. Fault reactivation and fluid flow along a previously dormant normal fault in the northern North Sea. Geology 28 (7), 595–598.
Wu, W., Zhao, Z., Duan, K., 2017. Unloading-induced instability of a simulated granular fault and implications for excavation-induced seismicity. Tunnelling Underground Space Technol. 63, 154–161.
Wassing, B.B.T., Van Wees, J.D., Fokker, P.A., 2014. Coupled continuum modeling of fracture reactivation and induced seismicity during enhanced geothermal operations. Geothermics 52, 153–164.
Wang, C., Elsworth, D., 2016. Numerical investigation of the effect of frictionally weak minerals on shear strength of faults. In: 50th US Rock Mechanics/Geomechanics Symposium. American Rock Mechanics Association.